International Journal Of
Industrial Electronics Control and Optimization
Print ISSN: 3517-2645
Online ISSN: 3568-2645
Homepage: https://ieco.usb.ac.ir/

Design Optimization and Thermal Analysis of a Dual Three-Phase PM Motor for Electric Vehicles

Javad Rahmani-Fard

Department of Electrical and Computer Engineering, Qom University of Technology, Qom, Iran
Corresponding author's email: rahmanifard@qut.ac.ir

Article Info

Article type:
Research Article

Article history:
Received: 2025-03-14
Received in revised form: 2025-04-16
Accepted: 2025-04-22
Published online: 22-Dec-2025

Keywords:
Thermal Analysis,
Dual three-phase machine,
Optimal design,
PM machine.

ABSTRACT

This paper presents a comprehensive investigation into the design principles and operational characteristics of dual three-phase permanent magnet (PM) machines. The study focuses on optimizing the winding arrangement and slot-pole combinations for enhanced performance and reliability. Through detailed analysis, an optimal configuration is proposed, and a dual three-phase machine based on this design is developed. The operational behavior of the machine is thoroughly examined under healthy conditions, with particular attention given to its thermal performance to ensure it can sustain high power density and output power without compromising reliability. The effectiveness of the proposed design and thermal analysis is validated through advanced simulation results, which demonstrate the motor's robust performance, efficiency, and ability to maintain stable operation under demanding conditions. Under natural cooling, the dual three-phase motor operates safely within its thermal limits, with a maximum winding temperature of 139.99℃, below the 180℃ insulation limit, and a maximum magnet temperature of 105.62℃, below the 150℃ limit. This research highlights the potential of dual three-phase PM machines for applications requiring high reliability and performance.

I. Introduction

With the increasing emphasis on environmental sustainability, developing clean transportation has become a global priority. Electric vehicles (EVs) stand out due to their high efficiency, low noise, and zero emissions [1]. Advancements in EV technology are closely tied to improvements in power system performance, enhancing reliability and reducing costs [2].

A critical aspect of EV powertrains is the reliability of electric drive systems. Traditional three-phase motors are vulnerable to faults, which can reduce torque, cause vibrations, and compromise safety [3]. To address these challenges, modern motor designs prioritize fault tolerance, allowing continued operation under fault conditions to ensure passenger safety [4].

This paper analyzes a dual three-phase permanent magnet motor with integrated fault detection. This system identifies faults and applies control strategies to maintain torque output, ensuring safe EV operation [5,6]. Dual three-phase motors offer benefits such as low torque ripple, high torque density, and compatibility with standard inverters [7].

Key advantages of dual three-phase motors include [6]:

- High Fault Tolerance: Continued operation even with winding failures.
- Simplified Fault Control: Low harmonic content and minimal unbalanced magnetic pull.
- Enhanced Fault Performance: Ability to handle additional loads and maintain output under fault conditions.

Since the introduction of fractional-slot concentrated winding motors in 1996, fault-tolerant multi-phase motors have seen increasing use in critical applications [1,2]. Research has focused on optimizing pole and slot numbers, refining winding configurations, and reducing losses while improving fault tolerance [8-11].

Innovations in materials, such as Soft Magnetic Composites (SMC), have enabled modular motor construction, reducing costs and improving flexibility [12]. More recently, dual-rotor permanent magnet machines have been explored for their improved fault-tolerant control capabilities, optimized torque, and efficiency [13-15].

Recent advancements over the past years in dual three-phase permanent magnet (PM) machines have concentrated on fault tolerance, thermal management, and control strategies.

In the area of fault-tolerant control and winding optimization, Huang et al. [13] proposed a triple-redundancy control strategy for dual three-phase PM motors that maintained 85% of rated torque under single-phase open faults, ensuring continuous operation. While effective in maintaining performance during faults, this approach increases inverter complexity and computational load for real-time fault detection. Similarly, Zhou et al. [4] introduced an MMF reconstruction method to suppress vibrations and reduce torque ripple by 40% during open-phase faults through harmonic cancellation. However, their method relies heavily on accurate motor parameter identification, making it sensitive to parameter variations. Moreover, Yoshida and Akatsu [12] analyzed winding structures and showed that a 30° phase shift in winding reduces current total harmonic distortion (THD) by 15%, thus improving efficiency. This improvement is limited by a trade-off between harmonic suppression and torque density, restricting applications in high-power motors.

Regarding thermal and efficiency improvements, Wang et al. [8] designed an aviation-grade dual three-phase PM motor with integrated liquid cooling, which kept winding temperatures under 130°C at 20 kW, enabling high power density. However, integrating the liquid cooling system increased weight and system complexity. Tang and Sha [15] developed a biplane virtual voltage vector for model predictive control (MPC) in flux-weakening operations, improving efficiency by 3% at high speeds. Nonetheless, this approach is susceptible to permanent magnet demagnetization at elevated temperatures.

In sensorless and high-speed applications, Liu et al. [2] proposed a position-error correction method for sensorless dual three-phase PMSMs, achieving position errors below 1° at medium speeds without encoders. However, performance declines at speeds under 10% of rated speed due to low back-EMF signals. Azadrou [16] optimized a high-speed bearingless induction motor with a multi-cage rotor for compressors, achieving 15,000 rpm with minimal magnetic interference suitable for oil-free applications. The trade-offs include complex rotor fabrication and increased iron losses at ultra-high speeds.

For control strategies in mono-inverter dual-parallel (MIDP) systems, Fadaie et al. [17] introduced a simplified MPC approach that reduces computation time by 45% compared to traditional FCS-MPC and achieves minimal torque ripple. However, this method depends on accurate load torque estimation for optimal performance.

While previous studies have enhanced fault tolerance and efficiency, few have addressed combined electromagnetic-thermal optimization for high power-density electric vehicle motors. This paper fills that gap by proposing a 24-slot/22-pole design with optimized winding and pole arc geometry, validating thermal safety with winding temperatures of 139.99°C and PM temperatures of 105.62°C under natural cooling. The design achieves 94% efficiency and low torque ripple of 2.1% without requiring complex cooling systems.

This paper builds on these advancements, offering a detailed analysis of dual three-phase permanent magnet motors for EV applications. By enhancing fault tolerance, thermal performance, and efficiency, this research contributes to the development of more reliable and sustainable electric drive systems.

II. Analysis of MMF in Multi-Phase Motor Windings

Ideally, multi-phase motors with symmetrical windings and currents create a circular rotating magnetic field. However, real-world factors like slot effects and inverter nonlinearities (dead-time) introduce spatial and time harmonics. These harmonics interact, creating spatiotemporal harmonic MMFs that negatively impact motor performance (torque, noise, vibration). Therefore, analyzing these harmonic MMFs is crucial for understanding multi-phase motor behavior, considering both symmetrical and asymmetrical winding configurations.

A. MMF of Symmetrical Multi-Phase Windings

According to the theory of AC motor winding functions, the MMF can be expressed as the product of the winding function and the current. The MMF of the *m*-th phase of a symmetrical n -phase motor is:

$$F_m(\varphi,t) = n_m(\varphi) i_m(t) \tag{1}$$

For concentrated full-pitch windings, as shown in Figure 1(a), the Fourier series representation of the winding function is:

$$n_m(\varphi) = \sum_{v=1}^{\infty} N_v \cos\left[v\left(\varphi - \frac{m-1}{n}2\pi\right)\right] \tag{2}$$

where N_v is the amplitude of the v -th harmonic winding, and $N_v = 2Nk_w k_{pv}\sin(v\pi/2)/(v\pi)$ for $v = 1,3,5,\ldots$.

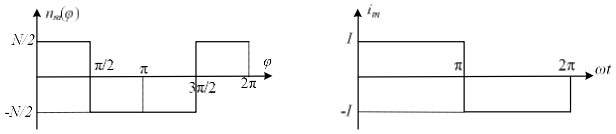

(a) (b)

Fig. 1. Winding function and phase current. (a) Winding function (b) phase current

The stator winding current is a 180° square wave, as shown in Figure 1(b). The *m*-th phase current can be expressed using the Fourier series as:

$$i_m(t) = \sum_{\mu=1}^{\infty} I_\mu \sin\left[\mu\left(\omega t - \frac{m-1}{n}2\pi\right)\right] \tag{3}$$

where ω is the angular frequency of the fundamental current, I_μ is the amplitude of the μ-th harmonic current, and $I_\mu = 4I/\mu\pi$.

Substituting equations (2) and (3) into equation (1), the MMF of the m -th phase of a symmetrical n-phase motor is:

$$F_m(\varphi,t)=\sum_{\nu=1}^{\infty}\sum_{\mu=1}^{\infty}N_\nu I_\mu\cos\left[\nu\left(\varphi-\frac{m-1}{n}2\pi\right)\right]\sin\left[\mu\left(\omega t-\frac{m-1}{n}2\pi\right)\right] \quad (4)$$

Therefore, the harmonic MMF generated by the μ-th harmonic current and the ν -th harmonic winding is:

$$F_{\nu\mu}(\varphi,t)=\sum_{m=1}^{n}N_\nu I_\mu\cos\left[\nu\left(\varphi-\frac{m-1}{n}2\pi\right)\right]\sin\left[\mu\left(\omega t-\frac{m-1}{n}2\pi\right)\right] \quad (5)$$

$$=\frac{nN_\nu I_\mu}{2}\left(F_{\mu\nu}\sin(\mu\omega t+\nu\varphi)+F_{\mu\nu}\sin(\mu\omega t-\nu\varphi)\right)$$

where:

$$F_{\mu\nu}=\frac{\sin[(\mu+\nu)\pi]}{n\sin[(\mu+\nu)\pi/n]}\quad F_{\mu\nu+}=\frac{\sin[(\mu-\nu)\pi]}{n\sin[(\mu-\nu)\pi/n]} \quad (6)$$

It can be seen that the harmonic MMF generated by the μ-th harmonic current and the ν -th harmonic winding consists of forward and backward traveling waves, and the condition for the existence of the resultant MMF is:

$$\mu\pm\nu=kn\quad k=0,\pm1,\pm2,\cdots \quad (7)$$

When the positive sign holds, the harmonic is a backward traveling wave; when the negative sign holds, it is a forward traveling wave. When both signs hold, it is a standing wave. The speed of the harmonic MMF is $\mu\omega/\nu$, meaning the speed of the harmonic MMF is proportional to the time harmonic and inversely proportional to the spatial harmonic.

B. MMF of Asymmetrical Multi-Phase Windings

The above analysis is for symmetrical multi-phase windings. Since asymmetrical multi-phase windings are composed of several sets of symmetrical windings shifted in space, the MMF of asymmetrical multi-phase windings can be analyzed using the superposition principle.

Assume an asymmetrical multi-phase winding consists of λ sets of n-phase symmetrical windings, each shifted by $\pi/(\lambda n)$ electrical degrees. The harmonic MMF generated by the μ-th harmonic current and the ν -th harmonic winding is:

$$F_{\mu\nu}(\varphi,t)=\sum_{i=1}^{n}N_i I_\mu\begin{pmatrix}\cos\left[\nu\left(\varphi-\frac{m-1}{n}\pi-\frac{i-1}{\lambda n}\pi\right)\right]\times\\ \sin\left[\mu\left(\omega t-\frac{m-1}{n}\pi-\frac{i-1}{\lambda n}\pi\right)\right]\end{pmatrix}$$

$$=\frac{\lambda nN_i I_\mu}{2}\left(F_{\mu\nu-}\sin(\mu\omega t+\nu\varphi)+F_{\mu\nu+}\sin(\mu\omega t-\nu\varphi)\right) \quad (8)$$

where:

$$F'_{\mu\nu-}=\frac{\sin[(\mu+\nu)\pi/(2n)]\sin[(\mu+\nu)\pi]}{\lambda n\sin[(\mu+\nu)\pi/(2n)]\sin[(\mu+\nu)\pi/n]} \quad (9)$$

$$F'_{\mu\nu+}=\frac{\sin[(\mu-\nu)\pi/(2n)]\sin[(\mu-\nu)\pi]}{\lambda n\sin[(\mu-\nu)\pi/(2n)]\sin[(\mu-\nu)\pi/n]} \quad (10)$$

It can be seen that for asymmetrical multi-phase motors, the condition for the existence of the harmonic MMF is:

$$\mu\pm\nu=k(2\lambda n)\quad k=0,\pm1,\pm2,\cdots \quad (11)$$

Similarly, when the positive sign holds, the harmonic is a backward traveling wave; when the negative sign holds, it is a forward traveling wave. For the 30° phase-shifted dual three-phase motor (asymmetrical six-phase motor) studied in this project, λ= 2 and n = 3. According to equation (9), $\mu\pm\nu=12k$. Comparing this with equation (5), it can be seen that the harmonic MMF distribution is the same as that of a symmetrical 12-phase motor, but the amplitude is halved.

Tables I and II show the harmonic MMF distributions for traditional 60° phase-band three-phase motors and dual three-phase motors, respectively. The MMF distribution of symmetrical six-phase motors is identical to that of three-phase motors, but the amplitude is doubled. The advantages of dual three-phase motors over three-phase and symmetrical six-phase motors are mainly reflected in the following two aspects:

1. Dual three-phase motors minimize torque ripple by eliminating 5th and 7th harmonic MMFs, resulting in the lowest harmonic MMFs being the 11th and 13th. This pushes the lowest torque ripple order to the 12th.
2. Dual three-phase motors lack standing waves. Injecting a 3rd harmonic current (with a single neutral point) can boost output torque, similar to symmetrical multi-phase motors.

TABLE I THE RESULTANT MMF FOR THREE-PHASE MOTOR

	Spatial harmonics generated by the winding (v)							
Current time harmonics (μ)		1	3	5	7	9	11	13
	1	1	×	-1/5	1/7	×	-1/11	1/13
	3	×	Standing Wave	×	×	Standing Wave	×	×
	5	-5	×	1	-5/7	×	5/11	-5/13
	7	7	Standing Wave	-7/5	1	Standing Wave	-7/11	7/13
	9	×	×	×	×	×	×	×
	11	-11	×	11/5	-11/7	×	1	-11/13
	13	13	×	-13/5	13/7	×	-13/11	1

TABLE II THE RESULTANT MMF FOR DUAL THREE-PHASE MOTOR

	Spatial harmonics generated by the winding (v)							
Current time harmonics (μ)		1	3	5	7	9	11	13
	1	1	×	×	×	×	-1/11	1/13
	3	×	1	×	×	×	×	×
	5	×	×	1	×	×	×	×
	7	×	×	-7/5	-5/7	1/3	×	×
	9	×	-3	×	1	×	×	×
	11	-11	×	×	×	1	×	-11/13
	13	13	×	×	×	-13/11	1	1

III. Determination of poles and slots

Dual three-phase motor design with concentrated windings requires specific stator slot numbers (multiples of 12 for symmetric distribution or Y dual-winding). Rotor pole pairs should match stator MMF harmonics (1, 5, 7, 11, 13 for symmetric; 1, 11, 13, 23, 25 for star). Rotor poles should be close to the number of teeth for a high winding factor, but excessive poles/slots are avoided for mechanical strength and motor size. The text then points to figures (2, 3, and 4) illustrating three example structures: 12-slot/10-pole (symmetric), 12-slot/10-pole (star), and 24-slot/22-pole (star).

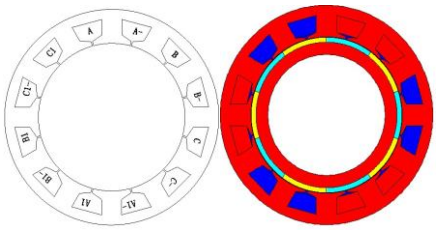

Fig. 2. Symmetric six-phase 12-slot/ 10-pole arrangement

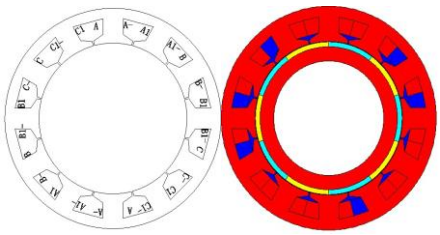

Fig. 3. Dual-star configuration with a 30-degree phase difference, 12-slot/ 10-pole arrangement

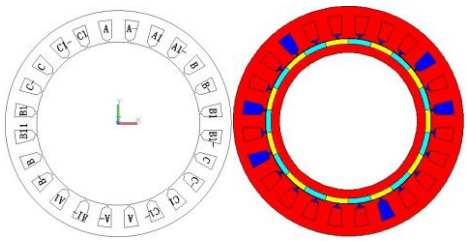

Fig. 4. Dual-star configuration with a 30-degree phase difference, 24-slot/ 22-pole arrangement

For the performance comparison of these three motors, their fundamental parameters are considered the same. These parameters include the volume of the iron core, the diameter of the stator, the air gap length, the axial length, the rated current, and the number of revolutions per phase. The other parameters extracted for these three motors are shown in Table III.

TABLE III COMPARISON OF PARAMETERS FOR THE THREE MOTORS

Parameters	12S/10P	12S/10P (Y30deg)	24S/22P
Winding factor	0.966	0.996	0.991
Average torque (N.m)	220.6	213.6	254.7
Torque ripple (%)	15.9	11.7	2.1
Peak short-circuit current (A)	48.5	76.7	25.4
Steel volume (m^3)	2.54×10^{-3}	2.54×10^{-3}	2.37×10^{-3}
Iron losses (W)	95.98	114.51	152.01
PM losses (W)	100.57	95.68	80.56

From the comparison of the above table, the following results can be extracted:

1) The dual three-phase motor with a 24-slot/ 22-pole single-layer winding has higher stator and rotor losses, but in other aspects such as average torque, torque ripple, and short-circuit current, it has superiority.

2) The 12-slot/10-pole design (compared to 24-slot/22-pole) requires a larger rotor and stator diameter, and a larger rotor yoke, due to the reduced number of poles. This lower pole number leads to greater interference between stator and rotor MMF harmonics, resulting in increased torque oscillations.

Therefore, the final structure is selected as the 24-slot/ 22-pole single-layer winding with a 30-degree phase difference.

IV. Optimization of no-load back-EMF

To optimize the no-load back-EMF, two methods are used: optimization of the pole arc coefficient and the inequality of the inner and outer iron core arcs.

A. Optimization of the pole arc coefficient

The pole arc coefficient is defined as the ratio of the pole shoe to the pole pitch. Since the number of slots and poles in the dual three-phase machine is close to each other, the pole pitch (slot to pole ratio) is almost one. By changing the pole arc coefficient, the main component and harmonic content of the back-EMF change, as shown in Figures 5 and 6.

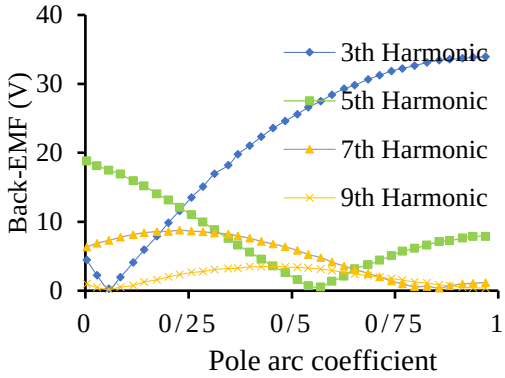

Fig. 5. Harmonic amplitude based on the pole arc coefficient

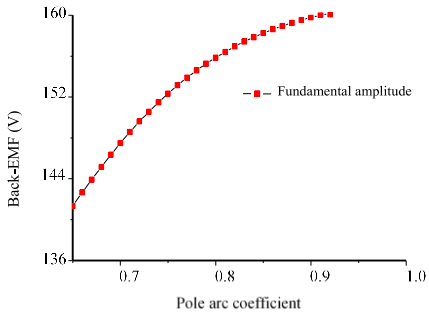

Fig. 6. Main component amplitude based on the pole arc coefficient

Figures 5 and 6 show that increasing the pole arc coefficient increases the main back-EMF component's amplitude, leveling off around 0.9. The 3rd harmonic is minimized at 0.67, and the 5th at 0.85. While the main component generates torque, the harmonics cause vibration and losses. Increasing the coefficient from 0.9 to 1 only improves the main component by 0.63% (small gain) but increases excitation current by 10%. Therefore, the optimal pole arc coefficient is 0.9. The back-EMF waveform shown in Figure 7.

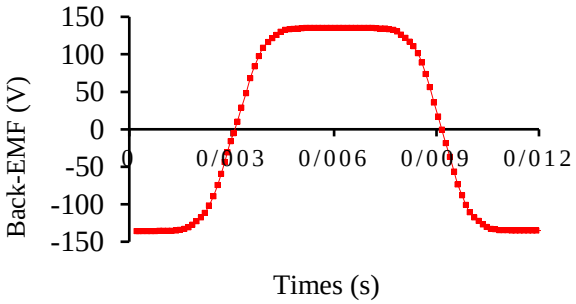

Fig. 7. Back-EMF waveform for a pole arc coefficient of 0.9

B. Permanent magnet eccentricity optimization

The inequality of the inner and outer PM arcs results in non-uniform air gap lengths. Therefore, the air gap flux is not a pure sine wave and becomes closer to a sinusoidal waveform. As a result, the back-EMF waveform becomes sinusoidal. However, due to the decrease in excitation current, the magnitude of the back-EMF also decreases. The difference in the inner and outer iron core arcs is shown in Figure 8.

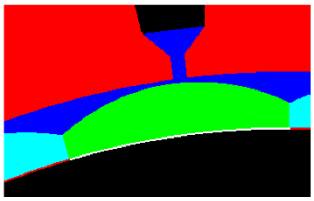

Fig. 8. Eccentric PM optimization

When the difference in the inner and outer iron core radii is 86 mm, the back-EMF waveform becomes the most sinusoidal, as shown in Figure 9.

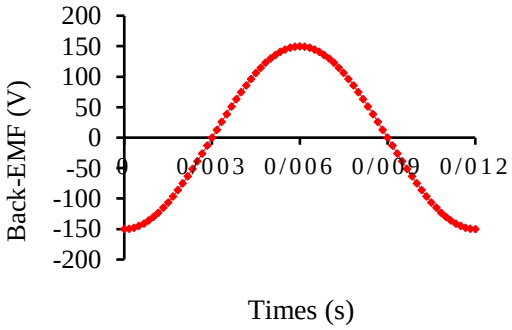

(a)

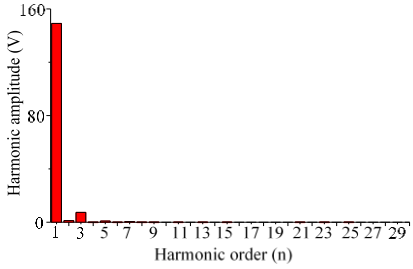

(b)

Fig. 9. (a) No-load back-EMF waveform with PM eccentricity optimization (b) Back-EMF harmonic spectrum

As observed, the waveform is sinusoidal with only a small amount of third harmonic. To evaluate the performance of this modified iron core configuration, it is compared with a conventional surface-mounted permanent magnet motor. For this comparison, the key parameters such as the outer diameter of the stator, axial length, rated current, and number of pole pairs are kept the same. Table IV shows the performance comparison of these two motors.

TABLE IV COMPARISON OF THE EFFECT OF PM SHAPE

Parameters	Conventional surface-mounted PM	Eccentric PM
Average torque (N.m)	254.7	211.1
Torque ripple (%)	2.1	0.24
No-load back-EMF (V)	159.75	150.1
Total Harmonic Distortion (THD)	12.8	2.4
Iron losses (W)	152.01	141.5
Volume of the PM (m^3)	2.64×10^{-4}	2.68×10^{-4}

Since using an iron core with unequal inner and outer arcs requires increasing the pole arc coefficient to enhance the permanent magnet flux, the leakage flux between the poles increases. This leads to a reduction in the no-load back-EMF and affects the motor's output torque.

Although the motor with this iron core shape has slightly lower torque ripple, its power generation capacity also decreases. Since torque ripple is not our main goal, the final structure of the motor is chosen to be a 24-slot/ 22-pole star-wound configuration with a 30-degree phase difference and a conventional iron core shape. The final dimensions of the main machine are specified in Table V.

TABLE V THE FINAL DIMENSIONS OF THE MAIN MACHINE

Parameters:	value
Outer diameter of the stator (mm)	350
Inner diameter of the stator (mm)	170
Axial length (mm)	109
Air gap length (mm)	0.6
Thickness of the PMs (mm)	5
Pole arc coefficient	0.9
Slots/pole	22/24
Number of turns per slot	80
Slot area (mm^2)	420

V. Analysis of Dual Three-Phase Motor Performance

When the motor operates under normal conditions, the motor torque, maximum torque, maximum speed, maximum power efficiency, and output characteristics are performance indicators of the motor. The nominal performance parameters of the motor are shown in Table VI. These values are investigated using finite element simulation in MAXWELL software. The nominal torque and maximum torque of the dual three-phase motor are shown in Figure 10.

TABLE VI PERFORMANCE PARAMETERS OF DUAL THREE-PHASE MOTOR

Number of Phases:	Dual Three-Phase
Nominal Voltage (V)	288
Nominal Power (kW)	12
Maximum Power (kW)	24
Nominal Speed (rpm)	450
Maximum Speed (rpm)	1200
Maximum Torque (N.m)	300
Maximum Efficiency	94%
Efficiency in the operational range above 80%	≥ 65%

When the effective current is 20 A, the nominal torque is obtained, and to reach the maximum torque, the effective current should be 23.6 Amperes.

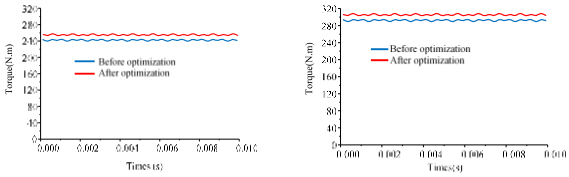

(a) (b)

Fig. 10. Output Torque (a) Nominal Torque (b) Maximum Torque

The cogging torque and iron losses of the motor are shown in Figures 11 and 12. Cogging torque is one of the problems of these motors that arises from the interaction between the rotor iron cores and the stator teeth. This torque causes vibration and noise during motor operation [17]. The peak cogging torque is 1.2 N.m, which is approximately 0.5% of the nominal torque. Additionally, the iron losses in the nominal torque are 152 W.

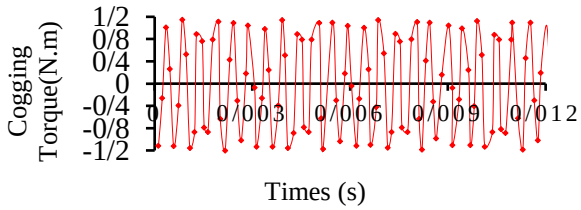

Fig. 11. Cogging Torque

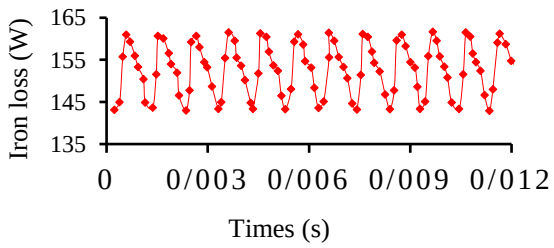

Fig. 12. Iron Losses

In an electric vehicle, achieving desired speed is important. In permanent magnet motors, rotor flux is constant and can't be reduced by field current. Above the nominal speed, induced EMF exceeds maximum input voltage, making current injection impractical. To solve this, air gap flux is weakened to limit induced EMF. Flux weakening is inversely proportional to stator frequency, keeping induced EMF constant as speed increases. For motor performance at speeds higher than the nominal speed, a specific flux weakening capacity is required. The flux weakening capacity depends ψ_s and $L_d i_s$ [18, 19]:

$$i_q = \frac{\sqrt{\left(u_{lim}/\omega\right)^2 - \left(L_d i_d + \psi_m\right)^2}}{L_q} \tag{12}$$

$$P = p i_q \omega \left(L_d i_d + \psi_m\right) \tag{13}$$

$$\omega = \frac{u_{lim}}{p\left(\psi_m - L_d i_d\right)} \tag{14}$$

where, ψ_m is rotor flux, L_d, L_q are inductances of q and d axes, i_d, i_q are currents of q and d axes, u_{lim} is voltage constraint, i_s is current constraint, p is number of pole pairs of the rotor and ω is angular speed.

when $\psi_m \approx L_d i_s$, the motor has the best flux weakening capability. In this motor, $\psi_m = 3.384\times10^{-2} Wb$, $L_d = 1.53 mH$, $i_s = 23.6A$, as result $L_d i_s = 3.384\times10^{-2} Wb$. Therefore, theoretically, this motor is in the best flux weakening condition. In the speed range below the rated speed, the reference value of ψ_m is equal to its nominal value, and in the flux weakening region (motor speed greater than rated speed), it changes inversely with speed, i.e. [20]:

$$\psi_m^{new} = \begin{cases} \psi_m, & n_r \le n_r^N \\ \dfrac{n_r^N}{n_r}\psi_m, & n_r^N \le n_r^N \le n_r^{max} \end{cases} \tag{15}$$

where ψ_m^{new} is the flux value in the flux weakening region, ω_{nom} is the rated speed (600 rpm), and ω_{max} is the maximum speed of the studied motor (1200 rpm). The speed-torque curve in the flux weakening region of the dual three-phase motor is extracted using MAXWELL simulation. Considering the design limitations, V_{max}=208V. Below the rated speed, i_d equals zero, and above the rated speed, the flux weakening strategy is employed. The efficiency constraint is such that the efficiency should be higher than 65% in more than 80% of the operating range. The motor efficiency map is shown in Figure 13.

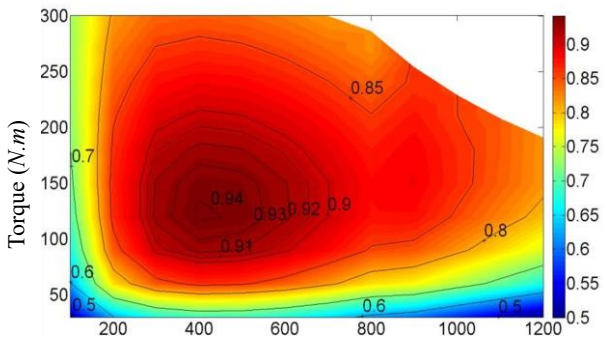

Fig. 13. Motor Efficiency Map

As seen from Figure 13, the maximum motor efficiency is 94.3%, which is higher than 94%, and in more than 80% of the operating range, the motor efficiency is around 71%,

which is higher than 65%. Therefore, the design considerations are taken into account. The motor efficiency at the rated operating point is approximately 90%.

VI. Thermal Rise Characteristics Analysis

Key to maximizing power density is ensuring thermal performance. The process involves: 1) calculating equivalent thermal conductivity coefficients, 2) creating a 3D model in Solidworks, and 3) analyzing the temperature field in Ansys.

A. Basic theory of heat exchange in dual three-phase motors

1) Heat Conduction

Heat conduction transfers energy between objects with a temperature difference, driven by microscopic particle movement. Heat flux density is proportional to the temperature gradient. The text implies an equation expressing this relationship is as

$$d\Phi = \lambda \frac{\partial T}{\partial n} dA \tag{16}$$

where, Φ is heat transferred, T is temperature of the part of the object being calculated, dA represents the micro-area at the specified point and λ is thermal conductivity coefficient of the material. Then, the relationship between heat flux density $\boldsymbol{q}$ and thermal conductivity is:

$$q = \frac{d\Phi}{dt} = -\lambda \frac{\partial T}{\partial n} \tag{17}$$

Eq (16) and (17) summarize the famous Fourier's Law. In equation (17), $\partial T/\partial n$ is the temperature gradient $grad\mathbf{T}$, thus, the thermal conductivity coefficient $\lambda = -q/gradT$.

2) Convection

Convection refers to the relative flow within a fluid due to temperature differences between its parts, where heat is transferred from one part of the object to another through fluid motion. Generally, heat dissipation within an object is based on Newton's Law of Cooling, equating the process to convection, i.e.,

$$q = a(T_1 - T_2) = a\Delta T \tag{18}$$

The heat flux density (q) is related to the heat transfer coefficient (a) and object temperature (T). In this motor, air in the air gap is the only cooling medium. For air, flow velocity dictates the heat transfer coefficient. Empirical Eq. (19) (valid for wind speeds 1-40 m/s) summarizes the relationship

$$\alpha = \alpha_0(1 + k\sqrt{v}) \tag{19}$$

where, α_0 is the heat transfer coefficient at zero gas velocity; and k is the correction coefficient obtained from experiments.

3) Radiation

Heat transfer inside the motor also involves radiation, though it can sometimes be negligible. Radiative energy transfer occurs via electromagnetic waves. According to the radiation law, the radiative energy $(s^{-1}m^{-1})$ is given by:

$$q = \sigma\upsilon(T^4 - T_0^4) \tag{20}$$

where, σ is the Boltzmann constant for a perfect black body, $\sigma = 5.7\times10^{-8} W/m^2 \cdot K$, υ is the physical parameter related to the surface condition of the heat-dissipating body.

B. Temperature Field Simulation of Dual Three-Phase Motor

1) Analysis of Heat Sources in Dual Three-Phase Motor

The dual three-phase motor in this study has a high electrical load, leading to significant copper losses in the windings, which is the main heat source. Fractional-slot concentrated windings create harmonic components in the stator magnetic field, causing eddy current losses in the rotor magnets and iron losses in the stator/rotor. Winding heat source is calculated using $P_{cu} = mI^2R$, while other losses are found via finite element simulation. Loss distribution is shown in Table VII.

TABLE VII LOSSES OF COMPONENTS INSIDE DUAL THREE-PHASE MOTORS

Heat Source	Loss (W)	Heat Generation Rate (W/m³)
Armature Winding	720	7,559,362
Stator Teeth	104.25	90,159
Stator Core	47.83	36,897
PMs	80.56	205,698

2) Selection of Thermal Conductivity and Heat Transfer Coefficients for Dual Three-Phase Motor

The motor is composed of various materials, including silicon steel sheets, permanent magnets, insulating materials, copper wires, and air, each with different thermal conductivity coefficients. The thermal conductivity coefficient λ represents a material's ability to conduct heat and depends on factors such as temperature and material type. The definition of thermal conductivity is given by:

$$\lambda = \frac{q}{gradT} \tag{21}$$

In practical engineering, temperature is considered a primary factor affecting the thermal conductivity of materials. For most materials encountered in engineering, the thermal conductivity is approximately linearly related to temperature, as

$$\lambda = \lambda_0(1 + bt) \tag{22}$$

where, λ_0 is the Thermal conductivity at 0°, b is the Correction coefficient obtained from experiments, related to the material. The thermal conductivity coefficients of different materials in the motor are listed in Table VIII.

TABLE VIII Gas thermal conductivity depends on molecular collision rate and intensity. Higher temperature increases

THERMAL CONDUCTIVITY COEFFICIENTS OF MATERIALS IN DUAL THREE-PHASE MOTOR

Material	Stator Core	Windings	PMs
Thermal Conductivity W/(m.K)	40.05	396	8.9

molecular speed and collision frequency, thus increasing thermal conductivity. Air's thermal conductivity increases with temperature. The relationship is given by:

$$\lambda = \lambda_0 \left(\frac{T}{273} \right)^n \tag{23}$$

where n is a constant, and for air, n=0.82. The thermal conductivity coefficients of air at different temperatures are shown in Table IX.

TABLE IX THERMAL CONDUCTIVITY OF AIR AT DIFFERENT TEMPERATURES

Temperature	0℃	20℃	40℃	60℃
Thermal Conductivity W/(m·K)	0.0234	0.0260	0.0281	0.0289
Temperature	**70℃**	**80℃**	**100℃**	**120℃**
Thermal Conductivity W/(m·K)	0.02916	0.0301	0.0321	0.0329

3) Temperature Field Analysis of Dual Three-Phase Motor

Based on the above analysis, a temperature field model for the 24-slot 22-pole dual three-phase motor was established. The three-dimensional model of the dual three-phase motor was created using Solidworks, and the temperature field analysis was performed using the finite element software Ansys. The three-dimensional model and the meshed grid are shown in Figure 14.

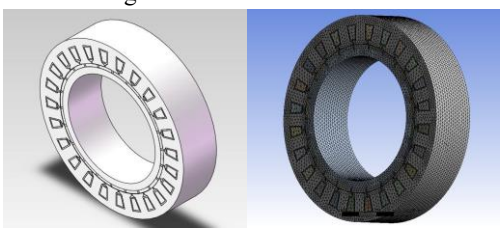

Fig. 14. 3D model and mesh generation of dual three-phase motors, (a) 3D model. (b) mesh generation results

From the temperature analysis results in Figure 15, the designed dual three-phase motor operates with temperatures ranging between 24.053℃ and 139.88℃ under natural cooling. The highest temperature, 139.99℃, occurs in the middle of the windings due to copper losses under rated conditions. The motor's class H insulation can withstand up to 180℃, ensuring no risk to winding insulation. The permanent magnets reach a maximum temperature of 105.62℃, well below their SH-grade heat resistance limit of 150℃, preventing damage or demagnetization. Thus, the motor operates safely within thermal limits.

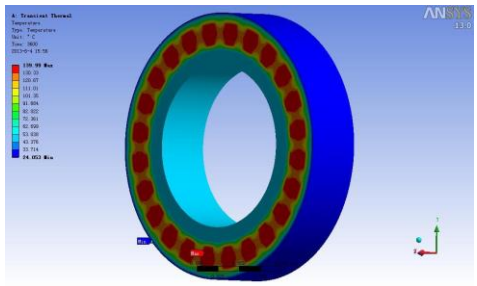

Fig. 15. Temperature field analysis results of dual three-phase motors

As summarized in Table X, our 24-slot/22-pole design demonstrates distinct advantages over contemporary solutions. While Huang et al.'s approach achieves fault tolerance at the cost of inverter complexity, and Wang et al.'s liquid-cooled system enables high power density with added weight, our optimized configuration delivers superior efficiency (94%) using natural cooling. This balanced performance profile - combining competitive torque output (254.7 N·m), minimal ripple (2.1%), and thermal stability (139.99°C windings) - positions our design as particularly suitable for mid-power EV applications where system simplicity and energy efficiency are paramount.

TABLE X COMPARATIVE SUMMARY OF THIS WORK VERSUS RECENT ADVANCES IN DUAL THREE-PHASE PM MACHINES

Study (Year)	Contribution	Advantage	Limitation
Huang et al. (2023)	3-redundancy fault-tolerant control	85% torque during faults	Complex inverter design
Wang et al. (2024)	Liquid-cooled aviation motor	20 kW at 130°C windings	Added weight/cost
This work	24-slot/22-pole + thermal optimization	94% efficiency, natural cooling	Limited to mid-power EV applications

VII. Conclusion

Compared to conventional electric machines, dual three-phase permanent magnet electric machines have more advantages such as high fault tolerance, simple control method under fault conditions, and good performance characteristics during faults. In this article, two winding configurations (star with 30-degree phase difference and symmetrical six-phase) were investigated for the dual three-phase motor. Based on harmonic analysis, the rules for selecting pole-slot combinations were extracted, and a comparison was made between the best possible configurations. It was shown that the 24-slot/ 22-pole structure with a star winding configuration and a 30-degree phase difference had superiority over other combinations. Then, the unloaded back-EMF was optimized. The results indicate that using an unequal iron core with inner and outer notches, although it makes the back-EMF waveform sinusoidal, it reduces the torque and motor power.

Furthermore, the internal temperature rise characteristics of the dual three-phase motor are analyzed, and the temperature field under steady-state conditions is studied.

REFERENCES

[1] H. T. Canseven, I. Petrov, and J. Pyrhönen, "Impact of Stator Core Magnetic Asymmetry on the Properties of a High Specific Power PMSM," IEEE Transactions on Industry Applications, vol. 60, no. 3, pp. 3830–3839, May 2024, doi: https://doi.org/10.1109/tia.2024.3357048.

[2] T. Liu, Z. Q. Zhu, X. Wu, Z. Wu, D. A. Stone, and M. P. Foster, "A Position Error Correction Method for Sensorless Control of Dual Three-Phase Permanent Magnet Synchronous Machines," IEEE Transactions on Industry Applications, vol. 58, no. 3, pp. 3589–3601, May 2022, doi: https://doi.org/10.1109/tia.2022.3152682.

[3] Y. Li, Z.-Q. Zhu, X. Wu, A. S. Thomas, and Z. Wu, "Comparative Study of Modular Dual 3-Phase Permanent Magnet Machines With Overlapping/Non-overlapping Windings," IEEE Transactions on Industry Applications, vol. 55, no. 4, pp. 3566–3576, Jul. 2019, doi: https://doi.org/10.1109/tia.2019.2908138.

[4] Y. Zhou, W. Zhao, X. Zhao, J. Ji, and Y. Sun, "Multi-Objective MMF Reconstruction Design for Vibration Suppression in Modular Dual 3-Phase PMSM With Open-Phase Fault," IEEE Transactions on Energy Conversion, pp. 1–10, 2024, doi: https://doi.org/10.1109/tec.2024.3479749.

[5] W. Huang, W. Hua, and Q. Fan, "Performance analysis and comparison of two fault-tolerant model predictive control methods for five-phase PMSM drives," CES Transactions on Electrical Machines and Systems, vol. 5, no. 4, pp. 311–320, Dec. 2021, doi: https://doi.org/10.30941/cestems.2021.00036.

[6] C. Zhang, Y. Wang, Z. Wu, W. Hua, and M. Zhang, "Implementation of Dual Three-Phase Linear Hall Sensor-Based Embedded Magnetic Encoder in Permanent Magnet Synchronous Motors," IEEE Transactions on Power Electronics, vol. 39, no. 9, pp. 10688–10692, Sep. 2024, doi: https://doi.org/10.1109/tpel.2024.3404848.

[7] M. Barcaro, N. Bianchi, and F. Magnussen, "Analysis and Tests of a Dual Three-Phase 12-Slot 10-Pole Permanent-Magnet Motor," IEEE Transactions on Industry Applications, vol. 46, no. 6, pp. 2355–2362, Nov. 2010, doi: https://doi.org/10.1109/tia.2010.2070784.

[8] J. Wang, L. Yan, X. Gao, and H. Su, "Electromagnetic thermal design and analysis of aviation dual three-phase permanent magnet machine," IET Conference Proceedings, vol. 2024, no. 13, pp. 2352–2357, Jan. 2025, doi: https://doi.org/10.1049/icp.2024.3382.

[9] D. Ishak, Z. Q. Zhu, and D. Howe, "Comparison of PM Brushless Motors, Having Either All Teeth or Alternate Teeth Wound," IEEE Transactions on Energy Conversion, vol. 21, no. 1, pp. 95–103, Mar. 2006, doi: https://doi.org/10.1109/tec.2005.853765.

[10] Y. Zhang et al., "Analysis of the Influence of Winding Phase Shift of Dual Winding Permanent-Magnet Synchronous Machines on Inter-turn Short Circuit Fault," Journal of Electrical Engineering & Technology, vol. 19, no. 8, pp. 5165–5176, Jun. 2024, doi: https://doi.org/10.1007/s42835-024-01934-4.

[11] J. Yu, W. Mi, Z. Cai, Z. Song, S. Liu, and C. Liu, "Design Principle Considering Structural Mutual Effects of Double-Stator V-Shape-PM Vernier Machines for Electric Ship Propulsion," IEEE Transactions on Transportation Electrification, vol. 10, no. 1, pp. 496–508, Mar. 2024, doi: https://doi.org/10.1109/tte.2023.3279202.

[12] A. Yoshida and K. Akatsu, "Study of Winding Structure to Reduce Harmonic Currents in Dual Three-Phase Motor," World Electric Vehicle Journal, vol. 14, no. 4, p. 100, Apr. 2023, doi: https://doi.org/10.3390/wevj14040100.

[13] L. Huang, W. Zhao, J. Ji, T. Tao, Y. Du, and Q. Zhang, "Enhanced Fault Tolerance of Dual Three-Phase Permanent Magnet Motor With Three-Redundancy Control," IEEE Transactions on Energy Conversion, vol. 38, no. 3, pp. 2211–2222, Sep. 2023, doi: https://doi.org/10.1109/tec.2023.3267786.

[14] K. Jankowska and M. Dybkowski, "Design and Analysis of Current Sensor Fault Detection Mechanisms for PMSM Drives Based on Neural Networks," Designs, vol. 6, no. 1, p. 18, Feb. 2022, doi: https://doi.org/10.3390/designs6010018.

[15] H.-Y. Tang, Q. Sha, and D.-Z. Xu, "Study on model predictive control of dual three-phase permanent magnet synchronous motor based on biplane virtual voltage vector," Archives of Electrical Engineering, pp. 869–890, Sep. 2024, doi: https://doi.org/10.24425/aee.2024.152100.

[16] Azadrou, H. . "Design and Optimization of a Very High Speed Three Phase Bearingless Induction Motor", International Journal of Industrial Electronics Control and Optimization, 6, 4, 2023, 283-289. doi: 10.22111/ieco.2023.45551.14.

[17] M. Fadaie , K. Abbaszadeh and A. Siadatan, "Simplified and Accurate Predictive Control Method in Mono-Inverter Dual-Parallel Permanent Magnet Synchronous Motors," International Journal of Industrial Electronics Control and Optimization, 5, 3, 2022, 251-260, doi: 10.22111/ieco.2022.41196.1405.

[18] Y. Wei, J. Si, Z. Cheng, S. Xu, L. Dong, and J. Liang, "Design and characteristic analysis of a six-phase direct-drive permanent magnet synchronous motor with 60° phase-belt toroidal winding configuration for electric vehicle," IET electric power applications, vol. 14, no. 13, pp. 2659–2666, Dec. 2020, doi: https://doi.org/10.1049/iet-epa.2020.0083.

[19] Sadiq Ur Rahman and C. Xia, "Rotor Speed and Position Estimation Analysis of Interior PMSM Machines in Low and Medium-High Speed Regions Adopting an Improved Flux Observer for Electric Vehicle Applications," Machines, vol. 11, no. 5, pp. 574–574, May 2023, doi: https://doi.org/10.3390/machines11050574.

[20] Y. Li and P. Gong, "Fault-Tolerant Control of Induction Motor with Current Sensors Based on Dual-Torque Model," Energies, vol. 16, no. 8, p. 3442, Apr. 2023, doi: https://doi.org/10.3390/en16083442.

Javad Rahmani-Fard received the B.S. degree from Shahed University, Tehran, Iran, in 2009, and the M.S. and Ph.D. degrees in electrical engineering from the K.N. Toosi University of Technology, Tehran, in 2012 and 2018, respectively. Currently, he is an assistant professor of the electrical engineering at Qom University of Technology, Qom, Iran. His research interests include the analysis and design of electrical machines, and sensor-less variable-speed drives, multiphase variable-speed drives.